SoRo

Soft Robotics

Unfolding Textile-Based Pneumatic Actuators for Wearable Applications

Ciarán T. O'Neill,[1,2] Connor M. McCann,[1,2] Cameron J. Hohimer,[1,2] Katia Bertoldi,[1] and Conor J. Walsh[1,2]

Abstract

Textile based pneumatic actuators have recently seen increased development for use in wearable applications thanks to their high strength to weight ratio and range of achievable actuation modalities. However, the design of these textile-based actuators is typically an iterative process due to the complexity of predicting the soft and compliant behavior of the textiles. In this work we investigate the actuation mechanics of a range of physical prototypes of unfolding textile-based actuators to understand and develop an intuition for how the geometric parameters of the actuator affect the moment it generates, enabling more deterministic designs in the future. Under benchtop conditions the actuators were characterized at a range of actuator angles and pressures (0–136 kPa), and three distinct performance regimes were observed, which we define as Shearing, Creasing, and Flattening. During Flattening, the effects of both the length and radius of the actuator dominate with maximum moments in excess of 80 Nm being generated, while during Creasing the radius dominates with generated moments scaling with the cube of the radius. Low stiffness spring like behavior is observed in the Shearing regime, which occurs as the actuator approaches its unfolded angle. A piecewise analytical model was also developed and compared to the experimental results within each regime. Finally, a prototype actuator was also integrated into a shoulder assisting wearable robot, and on-body characterization of this robot was performed on five healthy individuals to observe the behavior of the actuators in a wearable application. Results from this characterization highlight that these actuators can generate useful on-body moments (10.74 Nm at 90° actuator angle) but that there are significant reductions compared to bench-top performance, in particular when mostly folded and at higher pressures.

Keywords: textile-based actuators, pneumatic unfolding actuator, wearable robots, shoulder assistive device

Introduction

IN THE PAST decade, a wide range of wearable robots have been developed to assist with a variety of healthy and medical applications. One of the most commonly targeted medical applications is stroke rehabilitation, as strokes globally represent one of the most common causes of long-term upper limb disability, with 77.4% of stroke survivors developing an upper limb motor deficit.[1] As the first joint in the upper limb's kinematic chain, shoulder rehabilitation is of particular interest to clinicians and therapists.

It has been shown that robotic gravity compensation of the affected upper limb can lead to improved motor function as it off-loads and stabilizes the shoulder, allowing stroke survivors to focus instead on the smaller distal muscles of the elbow, wrist, and hand.[2–4] The robots used in these studies have typically been static rigid framed robots designed for research and clinical purposes.

In the search for lighter, more portable wearable robots, soft, frameless wearable robots that take advantage of the body's skeletal structure and joints have been developed by several groups.[5,6] This approach can apply assistance to a wearer's limb using remotely driven actuation modalities (thus enabling more optimal placement of heavy/rigid components on the body) and can achieve *mechanical transparency* when assistance is not required.

Some of these systems use electromechanical actuators coupled to compliant transmission mechanisms. Specifically, Bowden cable drives and twisted string actuators have been used to assist with walking[7–10] and upper limb movement.[11–19]

[1]John A Paulson School of Engineering and Applied Sciences, Harvard University, Boston, Massachusetts, USA.
[2]Wyss Institute for Biologically Inspired Design, Harvard University, Boston, Massachusetts, USA.

These electromechanical actuators can be deterministically designed in a stand-alone manner, although controlling and predicting the performance of the final wearable robot on the body can be a challenge due to the compliance of soft tissue and lack of fixed attachment points.[15,20,21]

In particular for cable-based shoulder robots,[11–15] the small biological moment arm over the deltoid may result in large reaction loads to be resisted by anchors unless an external structure is introduced to improve the effective moment arm. In contrast, an advantage of compliant cable-based actuation is that traditional force sensing can be used to control the force to modulate assistance to the wearer.

When cable-based actuation is not desired or suitable for an application, soft fluidic actuators may be used. Fluidic actuators can be lightweight, remotely actuated, and are inherently compliant when the fluid used is air or a similar gas. These actuators have most commonly consisted of a composite of fibers and elastomers, where the fibers limit strains in predetermined directions in the elastomer.[22–24] One of the most commonly used types of soft fluidic actuators is the pneumatic artificial muscle (PAM), which generates a linear tensile force when pressurized. PAMs have appeared in a range of wearable robots,[25–28] and due to their popularity, the modeling and control of PAMs have been well investigated in the literature.[29–32]

Non-PAM architectures for fluidic actuators also exist in the literature. Predicting the behavior of these non-PAM fluidic actuators has proved a challenge due to the large multidimensional deformations that the actuators typically undergo in addition to nonlinear material properties. However, work from a number of groups in recent years[23,33–35] has demonstrated successful modeling of a family of fiber reinforced elastomeric bending actuators, and we have seen their utility as an actuator in a soft robotic glove.[36–38]

To date, the majority of these soft fluidic actuators have relied on elastomeric materials. These elastomers typically exhibit a low stiffness to weight ratio, requiring thick walls which limit the minimum unpressurized volume and maximum power density of the actuators. Adding fibers to an actuator can result in improved power densities[37,39] as wall thickness can be reduced. This trend can be extended to use textiles, which are composed entirely of fibers, further improving the fluidic actuators' power density while minimizing wall thickness and weight. Textiles enable inflatable soft robots to be strong yet lightweight and compliant. Textile-based fluidic actuators which bend and rotate have been used in a number of wearable robots,[40–44] particularly in glove applications[45,46] where the low weight of the actuators minimizes the mass of the device on the hand.

Previous textile actuators developed in our group have used different modes of actuation, with bending and articulating actuators used for glove applications[47–49] and unfolding rotary actuators for the ankle and shoulder.[50,51] The bending actuators were constructed of knit materials and utilize differential stretching of the textile to create bending motions. This stretching may pose a challenge for higher force applications such as shoulder and ankle assistance, as it would result in excessive ballooning of the textile at higher pressures that may lead to failure. Thus, for systems intended to deliver higher levels of assistance, inextensible woven textiles are a viable option.

Finite element models have been used to predict the behavior and final shape of a range of elastomer-based inflatable actuators.[52–55] Existing models of textile-based actuators have typically been used for static structures[56–59] but there has been some recent work on finite element modeling of knitted textile actuators for wearable applications.[48,60]

Nesler *et al.*[61] and Fang *et al.*[62] both presented an elegant analytical approach for predicting the behavior of unfolding textile-based actuators by modeling the energetics of inflating the actuator. By assuming that the textile behaves as an inextensible membrane, they created a model that estimated the torque output of the actuator as a function of the fluidic input. The benefit of this approach is that it provides a very general methodology to modeling any fluidic actuator behavior, which is independent of the specific mechanism of actuation and the material properties of the actuator. However, approaches that include the specific moment generating mechanics at play in these actuators may help us improve our intuition of how they work.

An additional challenge with the design of soft inflatable actuators is that previous efforts in both modeling and experimental characterization assume idealized boundary conditions. When textile-based actuators are integrated into wearable applications, additional factors must be considered such as compliance introduced by the garment and the wearer soft tissue, as well as alignment with the biological skeleton.

In this work, we experimentally characterize a range of physical prototypes of unfolding textile-based actuators to improve our intuition and understanding of their underlying mechanics to better understand how design choices will impact performance. Driven by experimental characterization under ideal benchtop conditions, we developed a mechanics model that can be used to design similar actuators deterministically based on application requirements.

Finally, we extend our characterization to include on-body assessment so that the effect of the human-actuator interface can be understood and separated from the inherent behavior of the actuators on the benchtop. Collectively, these efforts will provide a foundation for a more robust understanding of the mechanism of operation of these unfolding actuators; the interactions between actuator and wearer; and provide guidelines for designing this class of actuators for wearable systems.

Actuator Design and Operating Theory

This work is focused on the unfolding textile-based pneumatic actuator shown in Figure 1. This is a simplified version of the actuator designed for our previous work in a shoulder assistive wearable robot,[50] which used a tapered multi-segment actuator. A simplified form of the actuator was chosen for this work to reduce the geometric parameter space describing the actuator and allow for clearer examination of the primary actuation mechanisms. This new understanding of the actuator mechanics lays the groundwork for both deterministic design of the actuators, as well as predicting and controlling the level of assistance, so that this can be correlated with muscle activity reductions of the users in future studies, which was not possible from our previous work.

The simplified actuator starts in a flat folded configuration, which unfolds when inflated. The actuator's cylindrical shell is constructed from a high stiffness woven textile with an
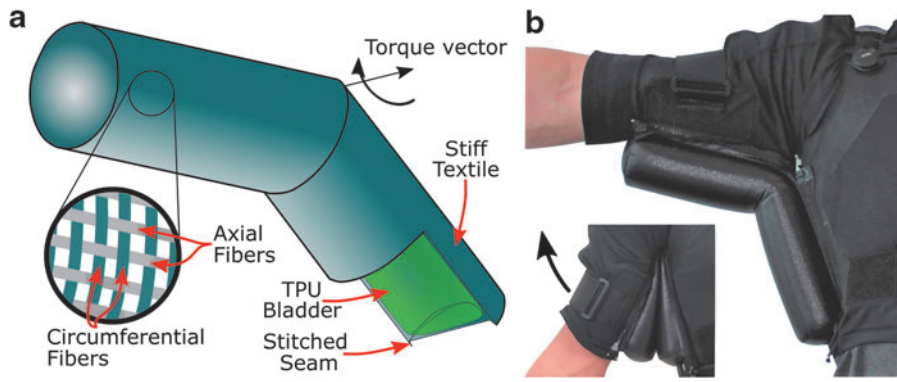
FIG. 1. **(a)** Structure of a textile-based pneumatic actuator. When pressurized, the actuator generates a clockwise moment about its axis of rotation. A magnified representation of the textile structure shows the alignment of the fibers of the textile with the circumference and axis of the actuator. **(b)** Actuator located in the axilla on a wearable device, abducting the arm from its rest position (as shown in the subfigure). Color images are available online.

internal bladder constructed of a flexible thermoplastic polyurethane membrane to provide an airtight volume. The textile is oriented with its fibers parallel to the radial and longitudinal axes of the actuator to ensure that one family of fibers typically resist the circumferential stress in the textile shell, while the orthogonal fiber family resists the longitudinal stresses. When a high stiffness textile is oriented in this manner, stretch of the textile during inflation is minimized.

By mounting the actuator within the axilla (Fig. 1b), the arm of the wearer is pushed upwards in abduction when the actuator inflates and unfolds, with the forces of actuation reacting against the torso and the medial upper arm. Locating the actuators within the axilla also limits the visual outline of the final wearable robot, potentially allowing it to be concealed below clothing. The bend in the actuator helps locate it within the axilla, while a long body helps distribute the forces of actuation to the wearer.

The general mechanism of actuation is similar to that of a bellows,[63] whereby a pressure acts upon two surfaces which are connected along one edge by a hinge, generating a moment about the hinge. The actuator's geometric parameters of radius, R, length, L, and pattern angle, φ (which refers to the maximum angle between the actuators fully folded state to its fully inflated state), are illustrated in Figure 2a. The current angle of the actuator is denoted by θ.

The force generated by the fluid across the actuator cross section (A_{cs}) is proportional to the fluid pressure and the cross-sectional area at a given angle. This pressure acts about the hinge axis with a moment arm (x_{cs}) at the section's centroid (Fig. 2a, red). The product of this moment arm (x_{cs}) and the cross-sectional area (A_{cs}) is the first moment of area. Thus, the overall moment produced is proportional to both the pressure and the first moment of area:

$$M\theta = PA_{cs}(\theta)x_{cs}(\theta). \tag{1}$$

$$M \propto PR^3. \tag{2}$$

As the actuator is deformed to angles other than the pattern angle, the expression for this first moment of area becomes more complex as the cross-sectional area becomes ovoidal, then truncated, and finally becomes rectangular when folded flat (see Supplementary Fig. S4 in the Supplementary Data for visualization). However, the underlying principle of moment generation remains unchanged.

Experimental Characterization Setup

To characterize effects of varying the geometric parameters on the generated moment, a base actuator was defined from which parameters would be varied. The selected geometric parameters in this work were the fundamental parameters required to describe the geometry of the actuator, its length, radius, and pattern angle. The length and radius of this base actuator were selected to replicate the dimensions of the
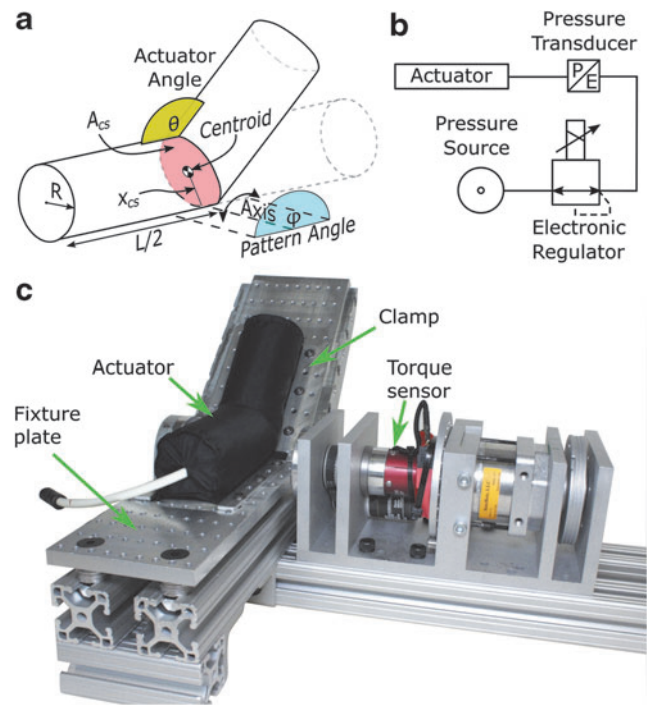
FIG. 2. **(a)** Geometric parameters of the textile actuator. In this example, the actuator has a length L and radius R and has a pattern angle of 180°. The angle θ is the current angle of the actuator relative to the fully folded position. The dashed outline represents the reference configuration. **(b)** Schematic for off-board fluidic supply. **(c)** Benchtop torque measurement rig. The actuator is coupled to the fixture plates using short sections of aluminum bar. The upper fixture plate is doubly supported and coupled to the torque sensor by a steel shaft. The angle between the plates can be indexed in 5° increments. Color images are available online.

actuators used in our previous work.[50] This resulted in an actuator with a radius of 25 mm and a length of 220 mm and a pattern angle of 180°.

To characterize the effects of length on actuator performance two variants (Nos. 1 and 2) of the base actuator were designed with lengths of 165 and 275 mm. As the moment generation is expected to scale with approximately the cube of the radius [Eq. (2)], three variants (Nos. 3–5) of the base actuator were prototyped with radii of 15, 20, and 30 mm. Finally, to investigate the effects of pattern angles less than 180°, three additional variants (Nos. 6–8) were prototyped with pattern angles φ of 90°, 120°, and 150°, respectively. All prototype actuators were fabricated using the method depicted in Actuator Fabrication section of the Supplementary Data Figure S1, and their dimensions are tabulated in Actuator Dimensions section of the Supplementary Data Figure S2.

To provide a consistent testing platform, an experimental apparatus was constructed to characterize prototype actuators. By characterizing the actuators in isolation, we could decouple the actuators' performance from any wearable robot on which they are used. The apparatus consisted of two main components: a fluidic actuation system (Fig. 2b) and a mechanical measurement rig (Fig. 2c).

The mechanical measurement rig pictured in Figure 2c was designed to measure the static torque output of an actuator. It included a torque sensor (TFF-350 500; Futek, USA) and plates that could be indexed and locked in 5° increments. The rigs range of angle between the plates was constrained to be between 15° and 210° due to part interference beyond these angles.

An off-board pneumatic supply (Fig. 2b) was used to control the fluidic input to the actuator during static characterization. Pressure regulation of the actuator was achieved using an electronic regulator (ITV1051-21N2BS4; SMC, Japan) and verified with an external pressure sensor (100PGAA5; Honeywell, USA). The use of pressure control compensates for any temperature variations and any air leakage from the bladder or connectors. Computer interfacing was achieved using two data acquisition units (DAQs) (NI6733 and NI6259; National Instruments, USA) in a target computer (ASUS B150-PLUS, ASUS, Taiwan) running xPC Target (MathWorks, USA). The DAQs were also used to read the torque sensor of the mechanical rig. Control of the system was implemented in Simulink (MathWorks, USA). All analog signals were recorded at 500 Hz.

A static characterization protocol was selected as the dynamic behavior of the actuators is highly dependent on the fluidic supply (the design of which was not the focus of this work). The static characterization protocol was performed on each actuator as follows. Actuators were first rigidly clamped in the test rig using simple clamps bolted to the fixture plates. The angle between the fixture plates was varied between 15° and the actuators maximum range-of-motion (ROM) in 15° increments using the index wheel. To capture sharp changes in the generated moment as a function of pattern angle φ, increments of 5° were used during the characterization of prototype Nos. 6–8. At each angle, the actuator was cyclically pressurized from 0 to 136 kPa (≈ 20 psi) at a rate of ±13.6 kPa/s for three cycles while the input pressure and output moment were recorded. The three cycles were averaged to produce a single curve for moment with respect to the rig angle for each actuator.

Experimental Characterization and Mechanism of Action

Actuator response

The results of the base actuator moment response as a function of angle and pressure can be seen in Figure 3a. As predicted by Equation (1), a linear relationship is observed between the generated moment and the pressure. A nonlinear relationship is observed between the actuator angle θ and its moment output. This nonlinear relationship is highlighted at different pressures in Figure 3b, and understanding the factors driving this response is critical. The magnitude of the nonlinearity is due to the significant variation in geometry between the fully folded actuator and its unfolded, fully inflated state. A sharp transition in the generated moment is also visible as the actuator approaches its pattern angle.

Through observation of the experimental tests, we can summarize the deformation of the actuator in three regimes, beginning with the actuator fully inflated at its pattern angle ($\varphi = 180°$), thus with predictable geometry and no deformation. In the first regime, Shearing, starting at its pattern angle at the right of Figure 3c, it was observed that as the actuator angle decreases, the actuator textile shears as shown in Figure 3c due to the low shear stiffness of the woven textile. This behavior is spring like, with a moment proportional to its angular deformation. As the actuator angle continues to decrease, it becomes energetically favorable for the actuator to crease/buckle, resulting in a sharp transition to the second regime (in the middle of Fig. 3c), Creasing, as this new deformation mode appears. We define the angle at which this transition occurs as the creasing angle, θ_{S-C}.

The formation of the crease and subsequent buckling is due to the presence of net compressive stresses in the textile which it cannot resist. These creases first appear on the top of the actuator, above the axis of rotation as depicted in Figure 3c, before growing deeper as the actuator angle decreases. The third regime (at the left of Fig. 3c), Flattening, involves a change in deformation mode from Creasing to Flattening and represents the behavior of the actuator at small angles, when there is significant contact between both halves of the actuator and large deformation of the actuator relative to its fully inflated state. The response of the actuator in this Flattening regime is pseudo-linear and begins at the transition angle θ_{C-F}.

Actuator modeling

Based upon the characterized moment generation response, an analytical model was derived for the mechanism of actuation to assist with our understanding of the mechanics at play. The predictions from this model are plotted alongside the experimental data for the base actuator in Figure 3b.

To capture the three distinct regimes of the actuator's behavior, a piecewise function was developed. The Shearing and Flattening regimes are modeled as linear functions to approximate the observed experimental responses of these regimes, with boundary conditions of M_{max} at $\theta = 0°$ and 0 at $\theta = \varphi$. A nonlinear function for the Creasing regime sits between both linear regimes, capturing the geometric nonlinearities of the creasing behavior, modeling the actuator output based on the first moment of area, the primary mechanism of actuation. This results in the piecewise formulation shown below:
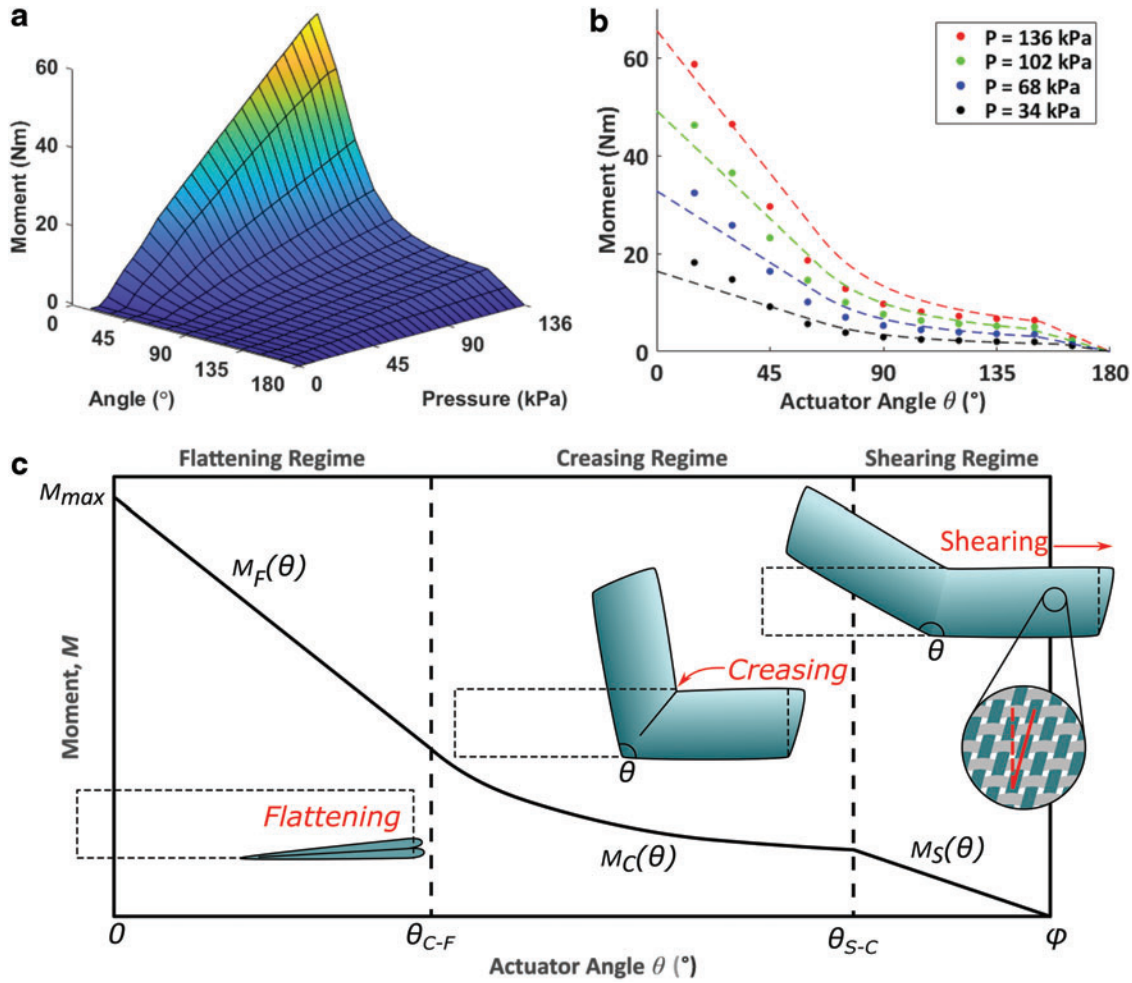
FIG. 3. **(a)** Full static characterization of the baseline actuator over all pressure and angles. **(b)** Isobaric moment response of the baseline actuator over the ROM of the actuator, analytical model represented as *dashed lines*, experimental data as points. **(c)** Breakdown of the generated moment across the three regimes observed. θ_{C-F} and θ_{S-C} denote angles at which the actuators transition from one regime to the next. ROM, range-of-motion. Color images are available online.

$$M(\theta) = \begin{cases} M_S(\theta) & \theta_{S-C} < \theta < \varphi \\ M_C(\theta) & \theta_{C-F} \leq \theta \leq \theta_{S-C} \\ M_F(\theta) & 0 < \theta < \theta_{C-F} \end{cases} \quad (3)$$

where:

$$M_S(\theta) = M_C(\theta_{S-C})\left(1 - \frac{\theta - \theta_{S-C}}{\varphi - \theta_{S-C}}\right). \quad (4)$$

$$M_C(\theta) = Pf(\theta, \{R, L, \varphi\}). \quad (5)$$

$$M_F(\theta) = M_{max} - \left(\frac{M_{max} - M_C(\theta_{C-F})}{\theta_{C-F}}\right)\theta. \quad (6)$$

See Analytical Actuator Model section of the Supplementary Data Figure S3 for further details on the calculation of θ_{C-F}, θ_{S-C}, M_{max}, and the nonlinear first moment of area function $f(\theta, \{R, L, \phi\})$. The piecewise model predictions were validated against the experimental results (dashed line

Figs. 3b and 4), with the model predictions following the observed trends and correlating well with the experimentally measured results, despite the simplicity of the geometric assumptions used. This model had a root mean square error (RMSE) of 3.6 Nm with respect to the No. 1 prototype actuator. Additional discussion of the model performance is included in Analytical Actuator Model section of the Supplementary Data.

Effect of parameter changes: length

The effect of actuator length was evaluated by comparing the experimental measured moment profiles of the base actuator with prototypes No. 1 and No. 2 ($L = 165$ and 275 mm, respectively). As seen in Figure 4a, the length significantly affects the moment response in the Flattening regime but plays a minimal role as the actuator angle increases. This can be explained by the fact that there is increased contact area in the Flattening regime, resulting from the additional length of the actuator, which significantly increases the first moment of area at small angles. When used in wearable applications, peak moment generation is seldom required at small
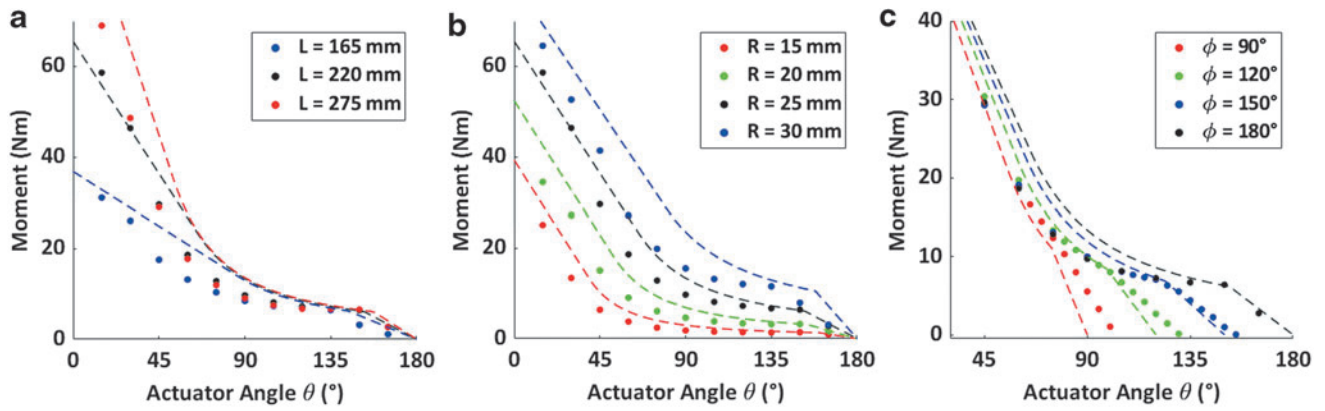
FIG. 4. **(a)** Effects of actuator length on static moment generation ($P = 136$ kPa). **(b)** Comparison of the experimentally measured moment to angle response to model predictions at 136 kPa with actuators of varying radius. **(c)** Effect of pattern angle on moment generation at 136 kPa. Analytical model represented as *dashed lines*, experimental data as points. Color images are available online.

actuation angles[64]; thus, design considerations regarding length are largely related to load distribution/comfort and its effects on volumetric requirements.

Effect of parameter changes: radius

To evaluate the effect of radius on the generated moment, prototypes (Nos. 3–5, R varying from 15 to 30 mm) were compared to the base prototype where it was observed that increases in actuator radius result in increased moment generation at all actuator angles (Fig. 4b). The mechanism of actuation in Equation (2) predicts a cubic relationship between radius and the generated moment, and a significant increase in generated moment is observed experimentally.

Effect of parameter changes: pattern angle

As they have identical radii, prototypes (Nos. 6–8, φ varying from 90° to 150°) exhibit identical moment responses during the Flattening and Creasing regimes until they reach their respective creasing angles (Fig. 4c). Once each actuator transitions from its Creasing regime to its Shearing regime, the generated moment diverges from moment response of the base actuator.

As observed in Figure 4c the actuators typically achieve a greater ROM than their pattern angle when fixed in the measurement rig due to minor asymmetric deformation upon inflation due to constraining the actuator to the fixture plate. When inflated without constraint, the pattern angle of the actuator closely matched the designed pattern angle.

Incorporation of Actuators into Wearable Devices

These textile-based pneumatic actuators are intended for use in soft wearable robots, in particular those that provide assistance with human motion. When designing these systems, actuators must be sufficiently sized to provide appropriate levels of assistance. Integrating actuators into a wearable system will introduce additional compliance (from apparel components and human tissue), as well as kinematic constraints. To better understand these effects, we performed additional characterization to quantify on body actuator performance.

In the mechanical measurement rig, the actuators were fixed to a pair of rigid planes that rotated exactly along the actuator's intended axis of rotation. In wearable applications, particularly for the shoulder, concentric alignment of an actuator's axis of rotation with that of the target joint may not be feasible as the joint's center of rotation is internal to the body (Fig. 5a). In addition, the compliance of the wearer's soft tissue and curved anatomy results in irregular contact between the actuator and wearer. Given that the angular position of the target joint is largely controlled by the input of the actuator, it is important to understand the relationship between the actuator angle and the target joint angle (the shoulder in this work). Specifically, given a desired range of motion or arm pose to assist, knowing the required actuator angle to achieve these goals would be beneficial to ensure that it can meet the desired torque requirements.

During initial experimentation in creating wearable systems with integrated actuators we observed that pattern angles close to 180° can result in uncomfortable point loading

FIG. 5. **(a)** Schematic diagram of actuator on human. When assisting the shoulder, there is a clear offset between the shoulder axis of rotation and that of the actuator. The compliance between the actuator and the upper arm must also be considered when considering the human-actuator interface. **(b)** Wearable robot tested in this work, highlighting the various elements. The base garment is constructed of a compressive athletic shirt. Color images are available online.
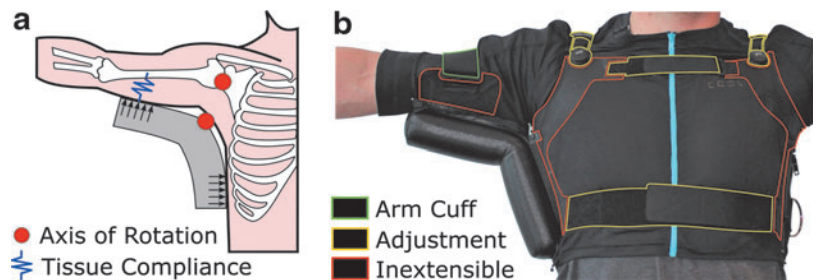
against the wearer at higher arm angles. During these conditions the actuator behaves more like an inflatable strut rather than an unfolding actuator, propping the arm up against the torso. By limiting the pattern angle of the actuator, this behavior can be mitigated, improving the comfort of the final design. According to the benchtop characterization, this reduction in pattern angle has no negative effects on moment generation at angles of interest for wearable assistance (i.e., in the vicinity of 90°). Thus, this is a simple modification that can be made to improve comfort.

Finally, the length of the actuator becomes more significant when used on-body. Longer actuators have the potential to be more comfortable as they allow for broader load distribution over a larger contact area compared to short actuators. Optimization of the final actuator length must balance comfort requirements and the fluidic supply requirements to power the actuator (since longer actuators will require more air volume).

Based on the above learnings, an actuator was designed to deliver the necessary moment (10.5 Nm[65]) to abduct the arm of a 50th percentile male[66] to 90°. Using the knowledge gained from the experimental characterization and analytical model, a radius of 29 mm was selected to deliver the requisite moment. The pattern angle of the actuator 150° was chosen to ensure that the actuator did not enter the Shearing regime ($\theta < \theta_{S-C}$) during the actuators expected ROM, since significant reductions in torque production were observed in this regime. The length of the actuator was selected for comfort to distribute the forces of actuation without affecting ROM or applying pressure to shallow subcutaneous vasculature and nerves. This resulted in the final actuator with the following parameters, $L = 290$ mm, $R = 29$ mm, $\varphi = 150°$. This actuator was characterized in the torque measurement rig to understand its performance in isolation.

Once the actuator had been created, the shirt component of the system was designed to provide adequate coupling of the actuator to the wearer, without restricting the wearers ROM. To efficiently secure the actuator in the axilla and provide the necessary assistance while minimizing restrictions, a harness system was constructed of a similar high-stiffness textile like that of the actuator. This harness was then integrated into a compressive athletic shirt (Fig. 5b). The harness component encircled the shoulder girdle and had an adjustable arm hole that could be tightened to locate the actuator axis of rotation as close as possible to the biological axis of rotation. The

harness was designed to pass over the acromion, a bony portion of the shoulder, to avoid applying reaction loads on the soft tissue of the deltoid or trapezius.

Adjustment straps were included in the front and back to fine tune the actuator's position and allow for load distribution across the garment. The actuator was coupled to the upper arm through an adjustable arm cuff, which is backed with a high-friction foam (Fabrifoam, USA) to prevent slippage of the cuff without excessive tightening. A front zipper was included for ease of donning.

On-Body Characterization

To characterize the on-body response of the actuator, the test fixture used for the benchtop experiments (Fig. 2c) was mounted to a column, and the rigid plates were replaced with a lever arm terminated with a padded arm cuff (Fig. 6a). On-body characterization was performed on five healthy male individuals (age [years]: 28.6 ± 3.6, height [m]: 1.77 ± 4.0, weight [kg]: 79.4 ± 2.6, body mass index: 25.3 ± 0.4) who appropriately fit the wearable device that had been fabricated. Due to the focus of this characterization on the actuator response rather than any biological effects, this on-body characterization involving human subjects was determined to be exempt by the institutional review board.

Before testing, participants donned the wearable system, and the fit was adjusted to ensure that the actuator was located correctly. Once the device was donned, the participant was secured to a chair with restraint straps to maintain their position during the characterization, and their arm was fixed into the arm cuff at the elbow (Fig. 6a). The lever coupling the arm cuff to the test fixture prevented lateral motion of the arm during actuator inflation, and the arm cuff also resisted internal and external rotation of the arm. The test rig's axis of rotation was adjusted to closely align with the axis of rotation of shoulder abduction. Close alignment of the axes ensured that the rig angle and the participants' biological arm angle were equivalent, and thus when indexing the rig angle, the arm angle was equally indexed.

Starting at an arm angle of 15°, the moment response of the actuator was characterized using the same protocol as the benchtop characterization, indexing every 15°. During each inflation cycle, at peak pressure, the effective actuator angle was recorded using a digital protractor (WR 410; Wixey, USA). Realignment of the test rig with the shoulder axis of
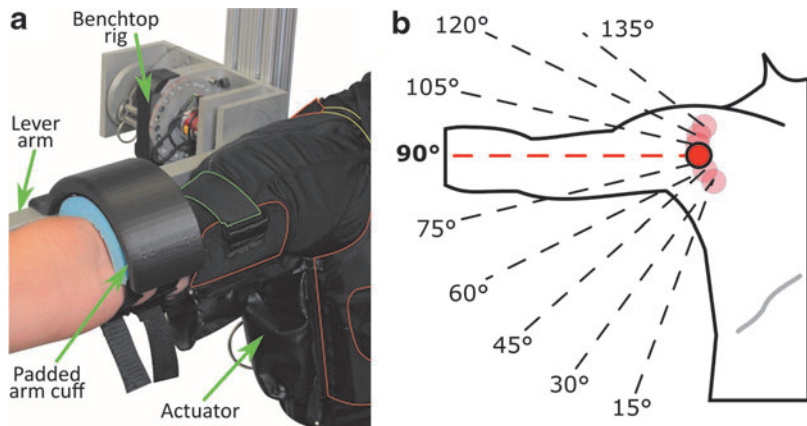
FIG. 6. (a) On-body characterization setup. A padded arm cuff was used for participant comfort and located at or proximal to the elbow. Both the rig's height and the location of the padded cuff along the lever arm were adjustable to allow for alignment between the participants shoulder and the rig's axis of rotation. (b) Range of arm angles evaluated with current arm angle of 90° highlighted. Color images are available online.
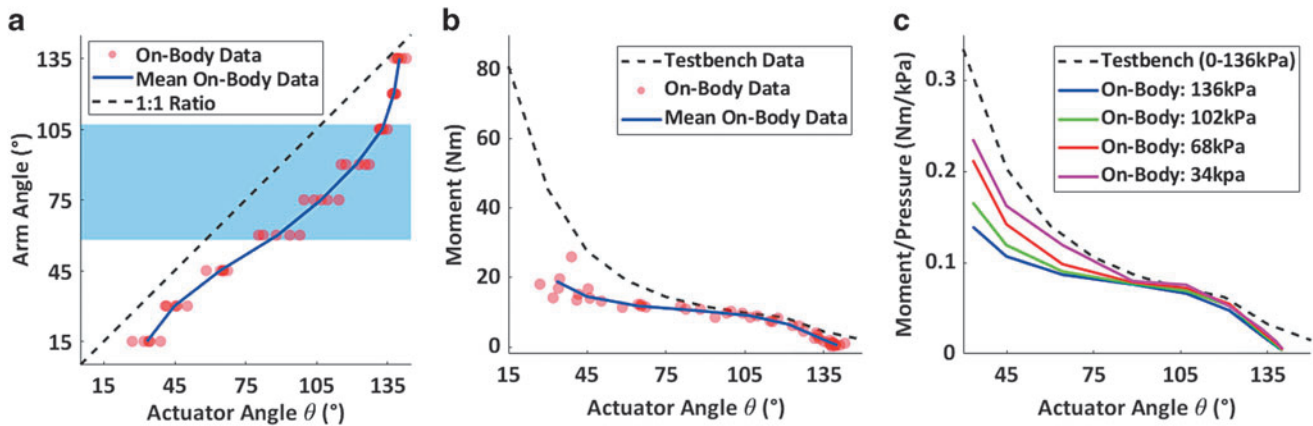
FIG. 7. **(a)** Average arm angle to actuator angle relationship at 136 kPa with range of variation greater than 25° highlighted in *blue*. **(b)** On-body moment response of the designed actuator compared to the test bench characterization of the same actuator at 136 kPa. **(c)** Normalization of the actuator's mean moment response with respect to pressure over a truncated actuator angle range reveals a nonlinear pressure relationship at low angles. Color images are available online.

rotation was performed as necessary as the arm angle was increased (Fig. 6b), up to a maximum arm angle of 135°.

The arm angle to actuator angle relationship is shown in Figure 7a. For the particular device tested, the most significant discrepancies between arm angle and actuator angle (maximum difference of $32.0° \pm 5.6°$) were observed in the arm angle range of 60° to 105°, which is the range in which the device is most likely to be operated. This highlights the importance of understanding the specific use case and the kinematics of an actuator when it is on the body in an integrated system.

Figure 7b shows the measured moments of the actuator across all healthy subjects. It can be seen that there is close agreement with the benchtop measurements at large actuator angles but significant deviation at low actuator angles. Figure 7c shows that there is greater deviation from the test bench data at higher internal actuator pressures. From observations during experiments, we believe that this may be due to out of plane motions of the actuator, meaning that only a component of the full actuator moment was serving to lift the arm. However, since the moment generation capabilities of the actuator at low angles far exceed the amount necessary to lift the arm, sufficient moment was still generated to successfully abduct the arm as designed in the expected operational range of the soft wearable robot.

Conclusion

A mechanism of actuation for unfolding textile-based pneumatic actuators is presented and validated in this work. The mechanism is geometry driven, based primarily on the effective first-moment-of-area of the actuator, and was experimentally validated with an array of physical prototypes of varying geometries. During this experimental characterization, three regimes (Shearing, Creasing, and Flattening) were clearly visible in each of the prototype actuators. The expected effects of the geometric parameters (radius, length, and pattern angle) were also clearly visible in the characterization. Based on the observed mechanisms of actuation, a piecewise model was developed to capture

the actuation mechanism. This model had a RMSE of 3.6 Nm with respect to the baseline prototype actuator characterized in this work.

Experimental on-body characterization was carried out to compare the actuators on-body behavior to their inherent behavior as captured by the benchtop characterization. Significant angular misalignment of the arm and actuator was observed due to the offset between the axes of rotation of the actuator and the target joint and soft tissue compliance at the human-actuator interface. This highlights the importance of understanding the geometry and anatomy of the target joint when designing these actuators for use in wearable robots.

Despite these effects, the measured on-body moments of the actuator were similar to those characterized on the benchtop, demonstrating that benchtop characterization can be a suitable method of characterizing components of soft wearable robots. In future work the dynamic behavior of the actuators on the benchtop and on-body will need to be characterized along with a dedicated wearable fluidic supply. Understanding dynamic effects such as hysteresis in the generated moment and actuator bandwidth will further our understanding of the behavior of the actuator in its specific application to soft wearable robots.

Collectively, this work provides a foundation for a more robust understanding of the interactions between actuator and wearer and provides some guidelines for designing this class of textile-based actuators for wearable systems.

Supplementary Material

Supplementary Figure S1
Supplementary Figure S2
Supplementary Figure S3
Supplementary Figure S4
Supplementary Figure S5
Supplementary Data

References

1. Lawrence ES, Coshall C, Dundas R, et al. Estimates of the prevalence of acute stroke impairments and disability in a multiethnic population. Stroke 2001;32:1279–1284.
2. Beer RF, Ellis MD, Holubar BG, et al. Impact of gravity loading on post-stroke reaching and its relationship to weakness. Muscle Nerve 2007;36:242–250.
3. Housman SJ, Otr L, Scott KM, et al. A randomized controlled trial of gravity-supported, computer-enhanced arm exercise for individuals with severe hemiparesis. Neurorehabil Neural Repair 2009;23:505–514.
4. Krabben T, Prange GB, Molier BI, et al. Influence of gravity compensation training on synergistic movement patterns of the upper extremity after stroke, a pilot study. J Neuroeng Rehabil 2012;9:1.
5. Ferguson PW, Rosen J (Eds.) Wearable Robotics: Systems and Applications; 1st ed. Cambridge, MA: Academic Press, 2020.
6. Peng Z, Huang J. Soft rehabilitation and nursing-care robots: A review and future outlook. Appl Sci 2019;9: 3102.
7. Kim J, Heimgartner R, Lee G, et al. Autonomous and portable soft exosuit for hip extension assistance with Online Walking and Running Detection Algorithm. In Proceedings of the IEEE International Conference on Robotics and Automation. Brisbane, QLD: IEEE, 2018, pp. 5473–5480.
8. Lee S, Karavas N, Quinlivan BT, et al. Autonomous multi-joint soft exosuit for assistance with walking overground. In IEEE International Conference on Robotics and Automation (ICRA). Brisbane, QLD: IEEE, 2018, pp. 2812–2819.
9. Bae J, Siviy C, Rouleau M, et al. A lightweight and efficient portable soft exosuit for paretic ankle assistance in walking after stroke. In Proceedings of the IEEE International Conference on Robotics and Automation. Brisbane, QLD: IEEE, 2018, pp. 2820–2827.
10. Mooney LM, Herr HM. Biomechanical walking mechanisms underlying the metabolic reduction caused by an autonomous exoskeleton. J Neuroeng Rehabil 2016;13: 1–12.
11. Gaponov I, Popov D, Lee SJ, et al. Auxilio: a portable cable-driven exosuit for upper extremity assistance. Int J Control Autom Syst 2017;15:73–84.
12. Galiana I, Hammond FL, Howe RD, et al. Wearable soft robotic device for post-stroke shoulder rehabilitation: identifying misalignments. In IEEE International Conference on Intelligent Robots and Systems. Vilamoura: IEEE, 2012, pp. 317–322.
13. Park D, Koo I, Cho KJ. Evaluation of an improved soft meal assistive exoskeleton with an adjustable weight-bearing system for people with disability. In IEEE International Conference on Rehabilitation Robotics. Singapore: IEEE, 2015, pp. 79–84.
14. Cappello L, Binh DK, Yen SC, et al. Design and preliminary characterization of a soft wearable exoskeleton for upper limb. In Proceedings of the IEEE RAS and EMBS International Conference on Biomedical Robotics and Biomechatronics. Singapore: IEEE, 2016, pp. 623–630.
15. Lessard S, Pansodtee P, Robbins A, et al. A soft exosuit for flexible upper-extremity rehabilitation. IEEE Trans Neural Syst Rehabil Eng 2018;26:1604–1617.
16. Popov D, Gaponov I, Ryu JH. Portable exoskeleton glove with soft structure for hand assistance in activities of daily living. IEEE/ASME Trans Mechatronics 2017;22:865–875.
17. Yi J, Chen X, Wang Z. A Three-dimensional-printed soft robotic glove with enhanced ergonomics and force capability. IEEE Robot Autom Lett 2018;3:242–248.
18. Kang BB, Choi H, Lee H, et al. Exo-Glove Poly II: A polymer-based soft wearable robot for the hand with a tendon-driven actuation system. Soft Robot 2019;6:214–227.
19. Bützer T, Lambercy O, Arata J, et al. Fully wearable actuated soft exoskeleton for grasping assistance in everyday activities. Soft Robot 2020;00:1–16.
20. Yandell MB, Quinlivan BT, Popov D, et al. Physical interface dynamics alter how robotic exosuits augment human movement: implications for optimizing wearable assistive devices. J Neuroeng Rehabil 2017;14:1–11.
21. Schiele A. An explicit model to predict and interpret constraint force creation in Phri with exoskeletons. In Proceedings of the IEEE International Conference on Robotics and Automation. Pasadena, CA: IEEE, 2008, pp. 1324–1330.
22. Hirai S, Cusin P, Tanigawa H, et al. Qualitative synthesis of deformable cylindrical actuators through constraint topology. In IEEE International Conference on Intelligent Robots and Systems. Takamatsu, Japan: IEEE, 2000, Vol. 1, pp. 197–202.
23. Bishop-Moser J, Krishnan G, Kim C, et al. Design of soft robotic actuators using fluid-filled fiber-reinforced elastomeric enclosures in parallel combinations. In IEEE International Conference on Intelligent Robots and Systems. Vilamoura: IEEE, 2012, pp. 4264–4269.
24. Galloway KC, Polygerinos P, Walsh CJ, et al. Mechanically programmable bend radius for fiber-reinforced soft actuators. In 16th International Conference on Advanced Robotics, ICAR, Montevideo, 2013, Vol. 105.
25. Sugar TG, He J, Koeneman EJ, et al. Design and control of RUPERT: A device for robotic upper extremity repetitive therapy. IEEE Trans Neural Syst Rehabil Eng 2007;15: 336–346.
26. Park YL, Santos J, Galloway KG, et al. A soft wearable robotic device for active knee motions using flat pneumatic artificial Muscles. In Proceedings of the IEEE International Conference on Robotics and Automation, 2014, pp. 4805–4810.
27. Wehner M, Quinlivan B, Aubin PM, et al. A lightweight soft exosuit for gait assistance. In Proceedings of the IEEE International Conference on Robotics and Automation, 2013, pp. 3362–3369.
28. Al-Fahaam H, Davis S, Nefti-Meziani S, et al. Novel soft bending actuator-based power augmentation hand exoskeleton controlled by human intention. Intell Serv Robot 2018;11:247–268.
29. Daerden F, Lefeber D. Pneumatic artificial muscles: actuators for robotics and automation. Eur J Mech Environ Eng 2002;47:11–21.
30. Villegas D, Van Damme M, Vanderborght B, et al. Third–generation pleated pneumatic artificial muscles for robotic applications: development and comparison with McKibben Muscle. Adv Robot 2012;26:1205–1227.

31. Versluys R, Deckers K, Van Damme M, et al. A study on the bandwidth characteristics of pleated pneumatic artificial muscles. Appl Bionics Biomech 2009;6:3–9.

32. Ching-Ping Chou, Hannaford B. Measurement and modeling of McKibben Pneumatic Artificial Muscles. IEEE Trans Robot Autom 1996;12:90–102.

33. Connolly F, Walsh CJ, Bertoldi K. Automatic design of fiber-reinforced soft actuators for trajectory matching. Proc Natl Acad Sci U S A 2017;114:51–56.

34. Wang Z, Polygerinos P, Overvelde JTB, et al. Interaction forces of soft fiber reinforced bending actuators. IEEE/ASME Trans Mechatronics 2017;22:717–727.

35. Bruder D, Sedal A, Bishop-Moser J, et al. Model based control of fiber reinforced elastofluidic enclosures. In Proceedings of the IEEE International Conference on Robotics and Automation. Singapore: IEEE, 2017, pp. 5539–5544.

36. Polygerinos P, Wang Z, Galloway KC, et al. Soft Robotic glove for combined assistance and at-home rehabilitation. Rob Auton Syst 2015;73135–73143.

37. Zhao H, Jalving J, Huang R, et al. A helping hand: soft orthosis with integrated optical strain sensors and EMG control. IEEE Robot Autom Mag 2016;23:55–64.

38. Paoletti P, Jones GW, Mahadevan L. Grasping with a soft glove: Intrinsic impedance control in pneumatic actuators. J R Soc Interface 2017;14.

39. Zhang J, Sheng J, O'Neill CT, et al. Robotic artificial muscles: Current progress and future perspectives. IEEE Trans Robot 2019;35:761–781.

40. Sridar S, Qiao Z, Muthukrishnan N, et al. A soft-inflatable exosuit for knee rehabilitation: Assisting swing phase during walking. Front Robot AI 2018;5:1–9.

41. Simpson CS, Okamura AM, Hawkes EW. Exomuscle: An inflatable device for shoulder abduction support. In Proceedings of the IEEE International Conference on Robotics and Automation. Singapore: IEEE, 2017, pp. 6651–6657.

42. Natividad RF, Hong SW, Miller-Jackson TM, et al. The Exosleeve: A soft robotic exoskeleton for assisting in activities of daily living. Biosyst Biorobotics 2019;22:406–409.

43. Park J, Choi J, Kim SJ, et al. Design of an inflatable wrinkle actuator with fast inflation/deflation responses for wearable suits. IEEE Robot Autom Lett 2020;5:3804–3810.

44. Simpson C, Huerta B, Sketch S, et al. Upper extremity exomuscle for shoulder abduction support. IEEE Trans Med Robot BIONICS 2020;2:474–484.

45. Yap HK, Khin PM, Koh TH, et al. A fully fabric-based bidirectional soft robotic glove for assistance and rehabilitation of hand impaired patients. IEEE Robot Autom Lett 2017;2:1383–1390.

46. Chu CY, Patterson RM. Soft robotic devices for hand rehabilitation and assistance: A narrative review. J Neuroeng Rehabil 2018;15:1–14.

47. Cappello L, Galloway KC, Sanan S, et al. Exploiting textile mechanical anisotropy for fabric-based pneumatic actuators. Soft Robot 2018;5:662–674.

48. Connolly F, Wagner DA, Walsh CJ, et al. Sew-free anisotropic textile composites for rapid design and manufacturing of soft wearable robots. Extrem Mech Lett 2019;2752–2758.

49. Zhou YM, Wagner D, Nuckols K, et al. Soft robotic glove with integrated sensing for intuitive grasping assistance post spinal cord injury. In Proceedings of the IEEE International Conference on Robotics and Automation. Montreal, QC: IEEE, 2019, pp. 9059–9065.

50. O'Neill CT, Phipps NS, Cappello L, et al. A soft wearable robot for the shoulder: design, characterization, and preliminary testing. In IEEE International Conference on Rehabilitation Robotics. London: IEEE, 2017, Vol. 02129, pp. 1672–1678.

51. Chung J, Heimgartner R, O Neill CT, et al. ExoBoot, a soft inflatable robotic boot to assist ankle during walking: Design, characterization and preliminary tests. In Proceedings of the IEEE RAS and EMBS International Conference on Biomedical Robotics and Biomechatronics, 2018, Vol. 2018-Augus, pp. 509–516.

52. Bishop-Moser J, Kota S. Design and modeling of generalized fiber-reinforced pneumatic soft actuators. IEEE Trans Robot 2015;31:536–545.

53. Polygerinos P, Wang Z, Overvelde JTB, et al. Modeling of soft fiber-reinforced bending actuators. IEEE Trans Robot 2015;31:778–789.

54. Bartlett NW, Tolley MT, Overvelde JTB, et al. A 3D-printed, functionally graded soft robot powered by combustion. Science 2015;349:161–165.

55. Shui L, Zhu L, Yang Z, et al. Energy efficiency of mobile soft robots. Soft Matter 2017;13:8223–8233.

56. Salama M, Lou M. Simulation of deployment dynamics of inflatable structures. AIAA J 2000;38:2277–2283.

57. Skouras M, Thomaszewski B, Kaufmann P, et al. Designing inflatable structures. ACM Trans Graph 2014;33:1–10.

58. Thomas JC, Bloch A. Non linear behaviour of an inflatable beam and limit states. Procedia Eng 2016;155398–155406.

59. Cavallaro PV, Smith RW. Conceptual inflatable fabric structures for protective crew quarters systems in space vehicles and space habitat structures. NUWC-NPT Tech Rep 2015;12:6–42.

60. Nguyen PH, Zhang W. Design and computational modeling of fabric soft pneumatic actuators for wearable assistive devices. Sci Rep 2020;10:1–13.

61. Nesler CR, Swift TA, Rouse EJ. Initial design and experimental evaluation of a pneumatic interference actuator. Soft Robot 2018;5:138–148.

62. Fang J, Yuan J, Wang M, et al. Novel accordion-inspired foldable pneumatic actuators for knee assistive devices. Soft Robot 2019;00:1–14.

63. Belforte G, Eula G, Ivanov A, et al. Bellows textile muscle. J Text Inst 2014;105:356–364.

64. Murray IA, Johnson GR. A study of the external forces and moments at the shoulder and elbow while performing every day tasks. Clin Biomech 2004;19586–19594.

65. de Leva P. Adjustments to Zatsiorsky-Seluyanov's segment inertia parameters. J Biomech 1996;29:1223–1230.

66. Fryar CD, Gu Q, Ogden CL. anthropometric reference data for children and adults: United States, 2007–2010. Natl Cent Heal Stat Vital Heal Stat 2012;11:2007–2010.

Address correspondence to:
Conor J. Walsh
John A Paulson School of Engineering
and Applied Sciences
School of Engineering Complex
150 Western Ave.
Boston, MA 02134
USA

E-mail: walsh@seas.harvard.edu

Supporting Information for
Unfolding textile-based pneumatic actuators for wearable applications

Ciarán T. O'Neill, Connor M. McCann, Cameron J. Hohimer, Katia Bertoldi, and Conor J. Walsh

S1   Actuator Fabrication

Actuators were fabricated as depicted in Figure S1. A CAD model is first generated according to the desired dimensions of the actuator (Figure S1(a)). These surfaces are than flattened (Figure S1(b)) and a seam allowance added to provide material to sew to (Figure S1(c)). These patterns are then laser cut (VLS6.60, Universal Laser Systems, USA) from a high-stiffness nylon plain-weave textile (Seattle Fabrics, USA). The pattern pieces are pinned together (Figure S1(d)) to ensure

(a) CAD model   (b) Flattened surfaces   (c) Seam allowance   (d) Sewing with pins for alignment

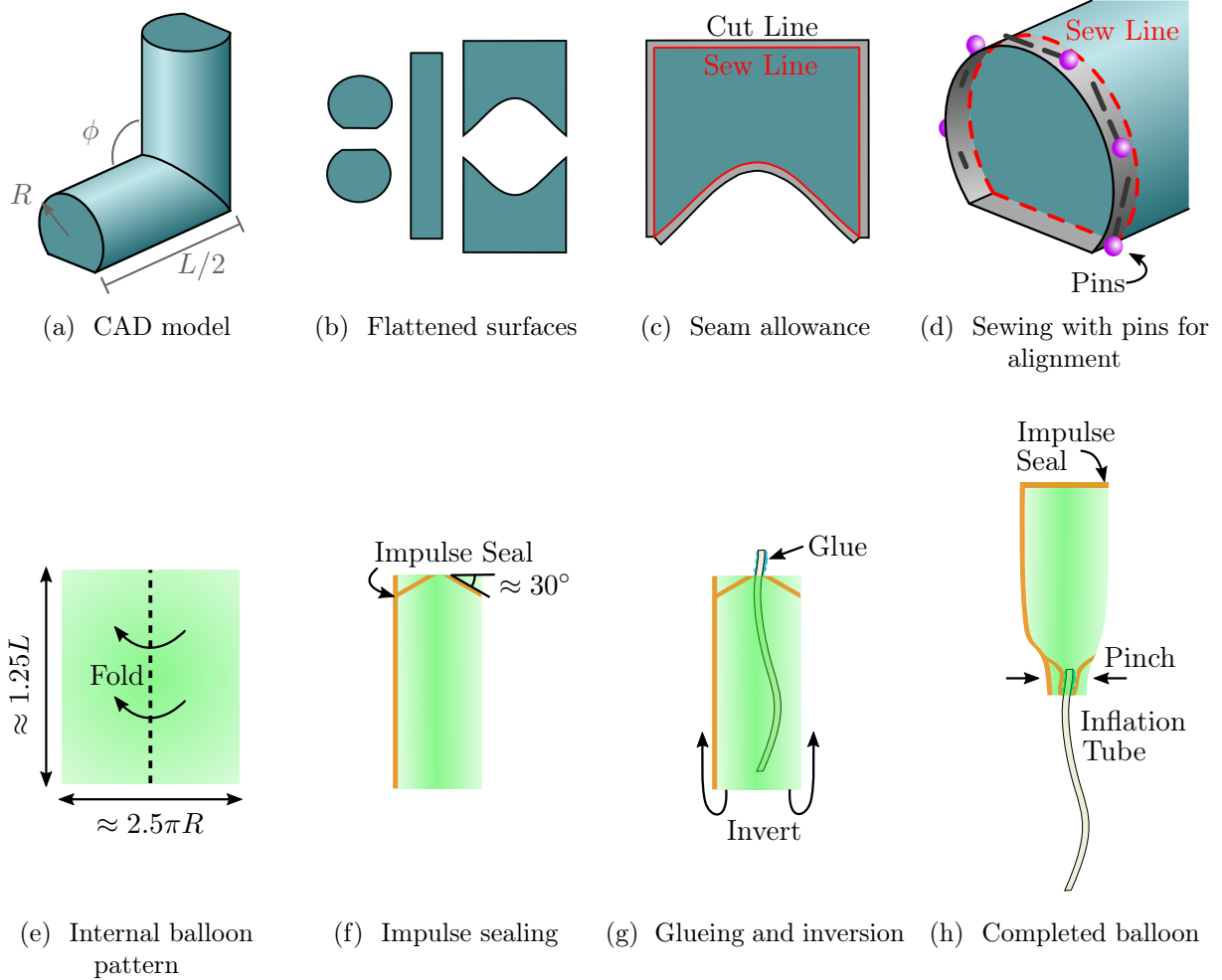(e) Internal balloon pattern   (f) Impulse sealing   (g) Glueing and inversion   (h) Completed balloon

Figure S1: Fabrication procedure for the actuators, including both the textile components (top) and the oversized internal thermoplastic balloon (bottom).

correct alignment when they are joined with a sewing machine (DDL-8700, Juki, Japan). Since the textile and sewn seams are not air-tight, internal thermoplastic bladders are inserted within the outer textile shell to contain the air. These bladders are cut from TPU (Stretchlon 200, Fiberglast, USA) to be $\sim 25\%$ oversized (Figure S1(e)) to ensure the textile is bearing all of the significant loads. The TPU sheet is folded lengthwise and then heat-sealed (Impulse foot sealer, American International Electric, USA) along the edge, creating a tube. A narrow opening is also formed for the air inlet (Figure S1(f)). A flexible tube (Parflex, Parker, USA) is inserted inside the bladder and glue (Vinyl, Fabric & Plastic Adhesive, Loctite, USA) is applied to its tip (Figure S1(g)) before the bladder is inverted and pinched to seal the tube in place (Figure S1(h)). The open end of the bladder is then heat-sealed before the bladders are inserted into the textile shell of the actuator.

S2   Actuator Dimensions

A series of actuators were prototyped to investigate the effect of the various design parameters. The details of these prototypes are listed below, with the design parameter being varied highlighted in bold:

Prototype	R (mm)	L (mm)	ϕ (°)	Description
0	25	215	180	Baseline
1	25	**165**	180	Length reduction
2	25	**270**	180	Length increase
3	**15**	215	180	Radius reduction (significant)
4	**20**	215	180	Radius reduction (minor)
5	**30**	215	180	Radius increase
6	25	215	**90**	Pattern angle reduction (significant)
7	25	215	**120**	Pattern angle reduction (intermediate)
8	25	215	**150**	Pattern angle reduction (minor)

Figure S2 shows three of the above prototypes fabricated for testing. Actuators #0, #3, and #7 are shown.

S3   Analytical Actuator Model

In order to better understand the underlying mechanisms of torque production in the actuators, a simplified analytical model was developed to capture the general trends observed in the bench-top experimental data. The objective for this model is not to capture every detail of the actuator deformation, but rather to make a first order approximation that allows for an understanding of general trends and underlying design principles. As such, the model can be utilized to understand the effect of the three design parameters (R, L, and ϕ, as presented in the main paper) on torque production.

For the sake of clarity, in the model, the reference (initial) configuration will be assumed to be the fully unfolded state (i.e. at the pattern angle, $\theta = \phi$, where θ is defined as shown in Figure S3), and an angular displacement will be applied to bend the actuator toward a fully folded state (i.e. decreasing θ) while a constant pressure, p, is maintained. This corresponds to the wearer's arm starting raised and pushing downward on the actuator. That said, the model is quasi-static and can therefore be applied to motions in either an upward or downward direction.

From the experimental data presented in Section VI of the main paper, three visually distinct angular regimes can be identified, each exhibiting a different torque profile and corresponding to a
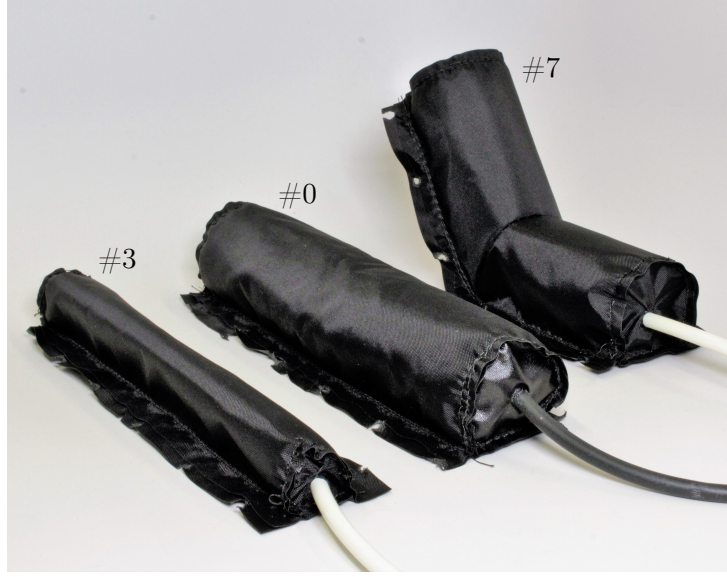
2

Figure S2: Three prototypes constructed for experimental testing, showing a range of design parameters.

different deformation mode of the textile structure (see Figure S3).

- In the Shearing Regime, the actuator exhibits a shear dominated deformation, as the top of the actuator translates laterally to accommodate the angular displacement imposed, while the bottom remains constrained to the testing apparatus. The resulting torque profile is linear, tending toward zero as θ goes to the pattern angle, ϕ (where the actuator is at equilibrium). In this regime, no creases are observed in the textile.

- The Creasing Regime starts when a crease forms in the center of the actuator at $\theta = \theta_{S\text{-}C}$. This crease gradually grows as the angular displacement is increased, resulting in a non-linear torque response. As soon as this crease forms, we have observed experimentally that the shearing seen in the first regime halts completely.

- Finally, in the Flattening Regime, the torque profile becomes linear once again, smoothly transitioning from the Creasing Regime at $\theta = \theta_{C\text{-}F}$. This corresponds to the actuator becoming fully compressed such that the end caps start to come into contact with each other. This leads to the actuator cross section becoming non-circular, and eventually at $\theta = 0$, the actuator has been fully flattened to a rectangular shape.

In the following sections we first introduce the parameters used to describe the geometry of the actuators and then present the model developed to describe their complex torque response, including the transition angles between the regimes ($\theta_{S\text{-}C}$ and $\theta_{C\text{-}F}$), the non-linear moment profile in the Creasing Regime ($M_C(\theta)$), and the maximum torque achieved when the actuator is fully compressed ($M_{\max}(\theta = 0)$).

S3.1   Actuator geometry

In the reference configuration the actuators considered in this paper consist of two cylindrical sections of radius R and length $L/2$ intersected at a "pattern angle" of ϕ (see Figure S4(a)). From these three design parameters, two derived lengths can be defined: $\tilde{L}$ and $\tilde{R}$.
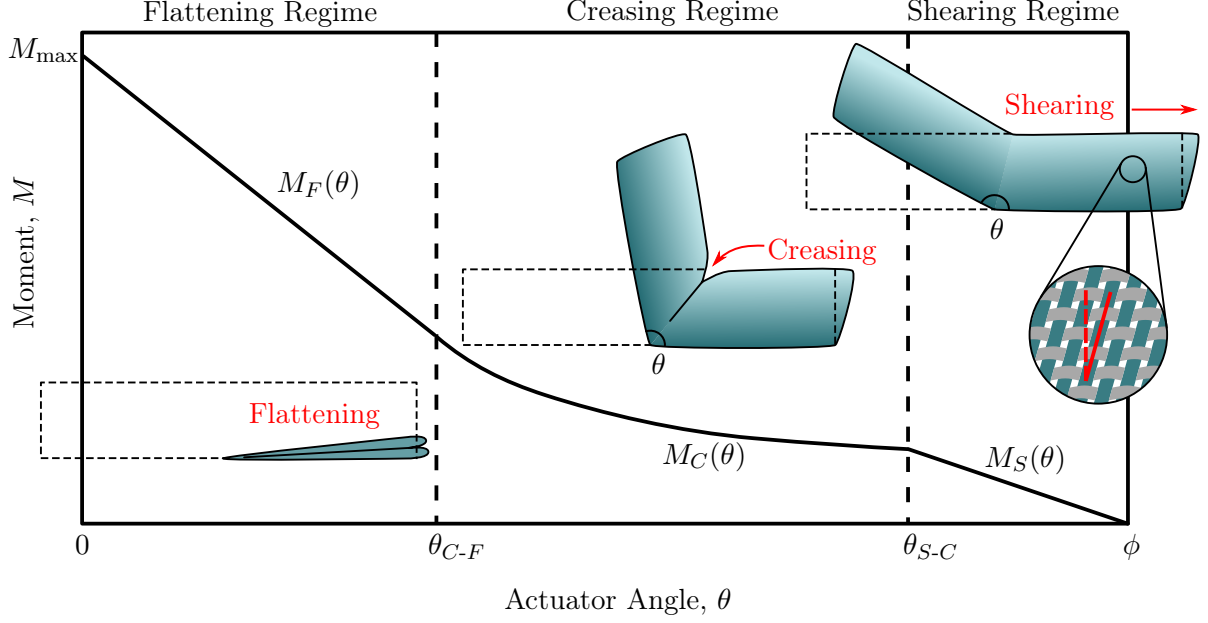
3

Figure S3: Representative actuator torque profile illustrating the three primary regimes.

$\tilde{L}$ is defined as the length of the actuator along the top edge (which is necessarily shorter than $L/2$ for $\phi < 180°$) and is given as:

$$\tilde{L} = \frac{L}{2} - 2R \cot \frac{\phi}{2}.$$ (1)

$\tilde{R}$ is the semi-major axis of the middle profile of the actuator (highlighted in blue in Figure S4(a)), which is an ellipse at an angle of $\phi/2$ with respect to each cylinder. Specifically, $\tilde{R}$ is given as:

$$\tilde{R} = R \csc \frac{\phi}{2}.$$ (2)

Moreover, the circumference of this ellipse is defined as s. Since a closed form expression does not exist for the circumference of an ellipse, the common Ramanujan approximation is employed:

$$s \approx \pi \left(3(R + \tilde{R}) - \sqrt{\left(3R + \tilde{R}\right)\left(3\tilde{R} + R\right)} \right)$$ (3)

In the deformed configuration (Figure S4(b)), the actuator experiences a combination of shearing and creasing. The shearing distance along the top edge of the actuator is defined to be δ, while the crease length is given as c. Additionally, the lengths a, b, and d are defined as shown in Figure S4(b), and will be utilized in the subsequent sections.

S3.2 Shearing Regime

The linear torque response observed in the Shearing Regime can be fully defined by the two endpoints $(\theta_{S\text{-}C}, M_C(\theta_{S\text{-}C}))$ and $(\phi, 0)$, and can be expressed as:

$$M_S(\theta) = M_C(\theta_{S\text{-}C}) \left(1 - \frac{\theta - \theta_{S\text{-}C}}{\phi - \theta_{S\text{-}C}} \right)$$ (4)

4

(a) Reference configuration

(b) Deformed configuration

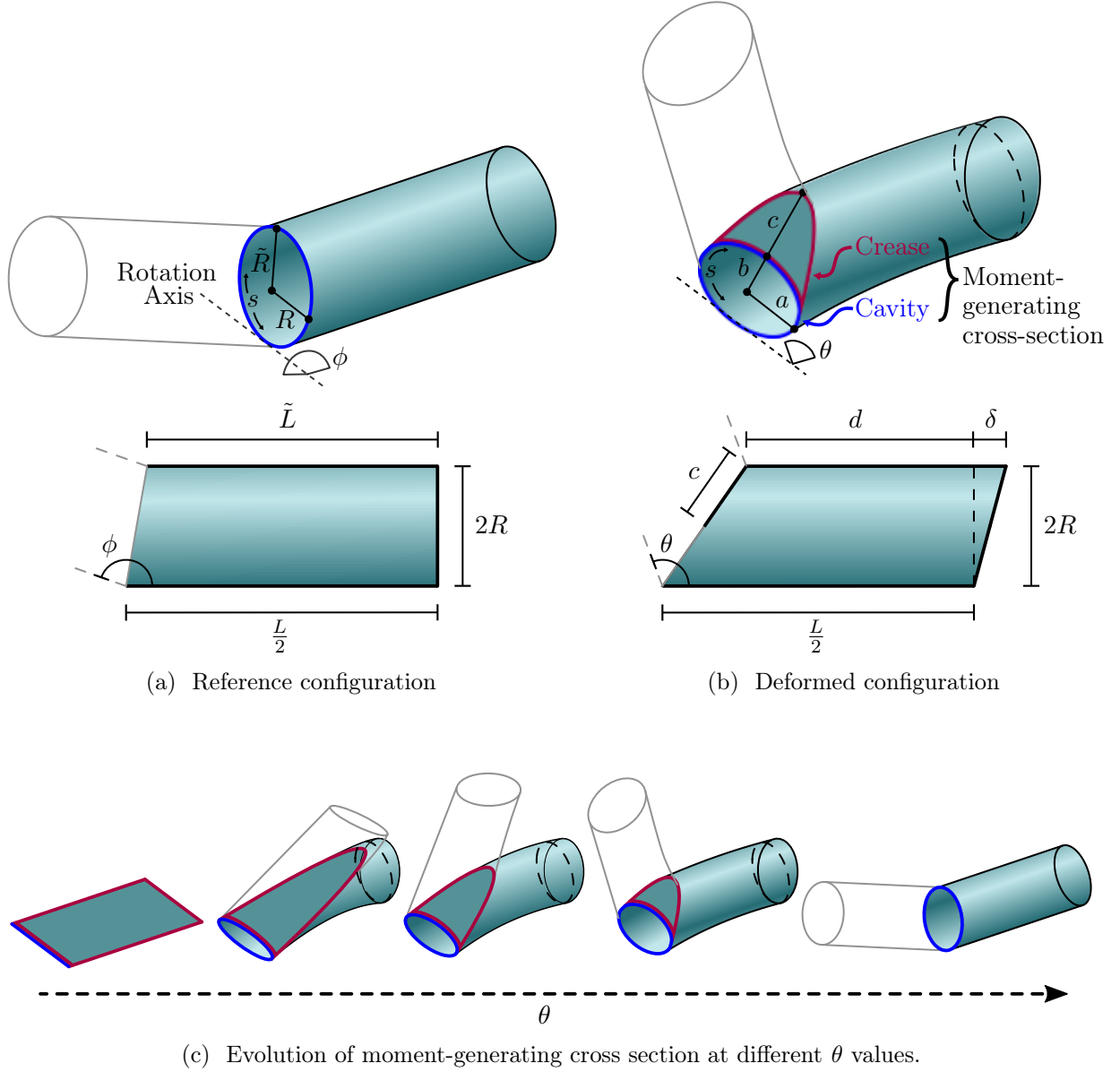(c) Evolution of moment-generating cross section at different θ values.

Figure S4: Approximate actuator geometry utilized in the analytical model.

While the exact form of $M_C(\theta)$ will be addressed in section S3.3, here we focus on identifying the critical angle $\theta_{S\text{-}C}$. This point occurs where it becomes energetically favorable for the actuator to transition from shear dominated deformation to the creasing behavior observed in the second regime. We posit that this corresponds to a trade-off between strain potential energy in the textile (which is required to shear the material) and flow work (which is required to push air out of the actuator when creasing occurs, as the volume of the actuator reduces).

To illustrate this concept, Figures S4(a) and S4(b) show simplified section views of the actuator in both the reference configuration as well a deformed state exhibiting both shearing and creasing, respectively. Because woven textiles exhibit much lower shear stiffness compared to in-plane stiffness, we assume that most of the deformation occurs through shearing and then creasing (rather than in-plane stretching) and that the material is therefore approximately inextensible in the plane.

5

In particular, we assume that when the actuator has sheared over by a distance δ, the top length of the actuator and its circumference (and therefore radius) remain unchanged. Moreover, we assume that a circular cross section is maintained until the crease forms. From these assumptions, we can calculate the derived length d labeled in Figure S4(b) with basic geometry as:

$$d = \frac{L}{2} - 2R \cot \frac{\theta}{2} \tag{5}$$

Since the deformations in the Shearing Regime are relatively small, we assume a linear elastic material with in-plane and shear moduli E and G, respectively. We do not assume the standard coupling between these two properties, since woven textiles exhibit much lower shear stiffnesses due to their internal structure. Given this material model, along with the geometric assumptions stated above, the shear stress τ takes the simple form

$$\tau = \frac{G\delta}{\pi R} \tag{6}$$

Moreover, the in-plane stresses are assumed to take the standard form for a cylindrical pressure vessel, yielding:

$$\sigma_{\text{axial}} = \frac{pR}{2t} \tag{7}$$

$$\sigma_{\text{hoop}} = \frac{pR}{t} \tag{8}$$

where t is the thickness of the textile. It follows that the strain energy density can be computed as:

$$\begin{aligned}
\Psi &= \frac{1}{2} \left(\frac{1}{E}\sigma_{\text{axial}}^2 + \frac{1}{E}\sigma_{\text{hoop}}^2 + \frac{2}{G}\tau^2 \right) \\
&= \frac{5p^2R^2}{8Et^2} + \frac{G\delta^2}{\pi^2R^2}
\end{aligned} \tag{9}$$

from which the total strain potential in the actuator is found as

$$W_s = \Psi V_m, \tag{10}$$

V_m being the material volume of the textile. Since it is assumed that the material in the crease does not contribute to the strain potential (as it is predominantly slack) V_m is given by

$$\begin{aligned}
V_m &= 2 \times (2\pi Rt) \left(\frac{\frac{L}{2} + (d + \delta)}{2} \right) \\
&= 2\pi Rt \left(L - 2R \cot \frac{\theta}{2} + \delta \right)
\end{aligned} \tag{11}$$

In addition to the strain potential, we must also consider the fluidic work done to push air out of the actuator

$$W_f = p\,\Delta V_f \tag{12}$$

where the change in fluidic volume ΔV_f is given by

$$\Delta V_f = V_{f,\text{ deformed}} - V_{f,\text{ reference}} \tag{13}$$

6

with

$$V_{f,\,\text{reference}} = 2 \times \pi R^2 \left(\frac{\frac{L}{2} + \tilde{L}}{2} \right) \tag{14}$$

$$V_{f,\,\text{deformed}} = 2 \times \pi R^2 \left(\frac{\frac{L}{2} + (d + \delta)}{2} \right) \tag{15}$$

Combining Equations (9)-(15), we can write the total energy in the system as:

$$
\begin{aligned}
W &= W_s + W_f \\
&= \Psi V_m + p\, \Delta V_f \\
&= \underbrace{2\pi R t \left(\frac{5p^2 R^2}{8Et^2} + \frac{G\delta^2}{\pi^2 R^2} \right) \left(L - 2R \cot\frac{\theta}{2} + \delta \right)}_{\substack{\text{Strain Term:} \\ \text{Increases with } \delta}} + \underbrace{p\pi R^2 \left(\delta - 2R \left(\cot\frac{\theta}{2} - \cot\frac{\phi}{2} \right) \right)}_{\substack{\text{Fluidic Term:} \\ \text{Decreases with } \delta}}
\end{aligned} \tag{16}
$$

Since the strain term in this expression increases with δ and the fluidic term decreases with δ, there is a unique $\delta(\theta)$ that minimizes the system energy:

$$\delta(\theta) = \arg\min_{\delta}(W(\theta)) \tag{17}$$

There is also a constraint on how large $\delta(\theta)$ can be, since the crease length, c, must be non-negative:

$$c \geq 0$$

$$2R \left(\cot\frac{\theta}{2} - \cot\frac{\phi}{2} \right) - \delta \geq 0$$

$$\delta_{\max} = 2R \left(\cot\frac{\theta}{2} - \cot\frac{\phi}{2} \right) \tag{18}$$

The critical angle $\theta_{S\text{-}C}$ occurs at the maximal θ value for which $c = 0$ (i.e. right before the crease forms). Thus, the following problem can be solved numerically:

$$\boxed{\theta_{S\text{-}C} = \arg\min_{\theta}(W) \quad \text{s.t.} \quad \{\delta(\theta) = \delta_{\max}\}} \tag{19}$$

To determine the material properties, values for $\theta_{S\text{-}C}$ were extracted from the experimental data presented in the main paper and used to fit the parameters E and G. It was found that (for the particular textile employed) values of $E = 36.4$ MPa and $G = 3.4$ MPa fit the experimental data best, with an RMS error of 6.0°on the $\theta_{S\text{-}C}$ prediction.

S3.3   Creasing Regime

Once the crease has formed in the middle of the actuator (i.e. for $\theta < \theta_{S\text{-}C}$), the torque profile becomes nonlinear in θ. Since it was observed experimentally that no further shear deformation occurs in this regime, and given that the material is assumed to be roughly inextensible, the prediction of actuator torque in this regime can be treated as a purely geometric problem. In particular, the torque transmitted from one half of the actuator to the other occurs purely as a result of the internal air pressure acting on the cross section geometry in the mid-plane of the actuator—i.e. both the internal cavity region (shown in blue in Figure S4(b)) and the crease region (shown in

7

red). Since the pressure in the actuator is known, a geometric model must be derived to predict the cross-sectional shape of the actuator in this regime.

For simplicity, the internal air cavity that makes up part of the moment-generating cross section is approximated as an ellipse, while the creased region is approximated by a parabola. While this is only a first-order approximation of the cross section, it simplifies the analysis since we need only derive expressions for the lengths a, b, and c in Figure S4(b), which fully define this geometry. Through basic geometry we can find that:

$$c + 2b = 2R \csc \frac{\theta}{2}$$
$$c = 2R \csc \frac{\theta}{2} - 2b \tag{20}$$

Due to the inextensibility assumption, the top length of the actuator ($\tilde{L}$, which was derived in Equation (1)) is required to remain constant between the reference and deformed configurations. This constraint is written below and then simplified using Equation (20) and the fact that δ remains fixed at $\delta_{\max}$ after the Shearing Regime:

$$\tilde{L} \equiv c + d + \delta$$
$$\tilde{L} \equiv 2R \csc \frac{\theta}{2} - 2b + d + \delta_{\max}$$
$$b = \frac{1}{2} \left(2R \csc \frac{\theta}{2} + d + \delta_{\max} - \tilde{L} \right) \tag{21}$$

To solve for the final cross-sectional dimension, a, we take advantage of the inextensibility assumption, which implies that the circumference of the elliptical air cavity, s, as defined in Equation (3), remains the same length in the reference and deformed configurations. Here the Ramanujan approximation for the circumference of an ellipse is again employed:

$$s \equiv \pi \left(3(a+b) - \sqrt{(3a+b)(3b+a)} \right)$$
$$a = \frac{1}{6\pi} \left(3s - 4\pi b + \sqrt{3s^2 + 12\pi bs - 20\pi^2 b^2} \right) \tag{22}$$

Now the geometry of the actuator cross section has been fully specified with parameters a, b, and c in Equations (22), (21), and (20), respectively. To compute the moment generated by the actuator, the internal pressure must be multiplied by the first moment of area, Q, of the cross section, taken about the appropriate rotational axis, as shown in Figure S4(b). To do this, the equations for the parabolic and elliptical portions of the cross section were written out explicitly, and a first-moment integral was performed:

$$y_e(x) = b - \frac{b}{a} \sqrt{a^2 - x^2}$$
$$y_p(x) = 2b + c - \frac{b+c}{a^2} x^2$$
$$Q = \int_{-a}^{a} \int_{y_e}^{y_p} y \, dy \, dx$$
$$= \frac{2}{15} a \left(9b^2 + 18bc + 4c^2 \right) + \frac{1}{2} \pi ab^2 \tag{23}$$
$$\boxed{M_C(\theta) = p \, Q(\theta)} \tag{24}$$

8

S3.4 Flattening Regime

In the final regime, the torque response of the actuators is once again approximately linear, and can be fully defined by the two endpoints $(0, M_{\max})$ and $(\theta_{C\text{-}F}, M_C(\theta_{C\text{-}F}))$ as:

$$M_F(\theta) = M_{\max} - \left(\frac{M_{\max} - M_C(\theta_{C\text{-}F})}{\theta_{C\text{-}F}}\right)\theta \tag{25}$$

To predict the maximum moment, $M_{\max}$ achieved at $\theta = 0$, we again estimate the the actuator geometry, compute a first moment of area, and multiply by the internal pressure. In this case, the geometry is easy to predict, as the tube has become fully flattened and is simply a rectangle of length $\frac{L}{2}$ and width πR (i.e. half the circular circumference). The first moment of area and moment produced can then be written as:

$$Q = \int_{-\frac{\pi R}{2}}^{\frac{\pi R}{2}} \int_0^{\frac{L}{2}} y \, dy \, dx$$

$$= \frac{\pi R L^2}{8}$$

$$M_{\max} = \frac{p\pi R L^2}{8} \tag{26}$$

Finally, the angle $\theta_{C\text{-}F}$ where the Creasing Regime transitions into the Flattening Regime can be predicted given the constraint that $M_C(\theta)$ be smooth and continuous with $M_F(\theta)$, which yields:

$$\theta_{C\text{-}F} = \theta' \quad \text{s.t.} \quad \left\{\frac{M_C(\theta') - M_{\max}}{\theta'} = \left(\frac{dM_C}{d\theta}\right)\bigg|_{\theta'}\right\} \tag{27}$$

S3.5 Summary of Equations

For convenience, all of the relevant equations for the model are summarized below.

$$M(\theta) = \begin{cases} M_S(\theta) & \theta_{S\text{-}C} < \theta \le \phi \\ M_C(\theta) & \theta_{C\text{-}F} < \theta \le \theta_{S\text{-}C} \\ M_F(\theta) & 0 < \theta \le \theta_{C\text{-}F} \end{cases}$$

where:

$$M_S(\theta) = M_C(\theta_{S\text{-}C})\left(1 - \frac{\theta - \theta_{S\text{-}C}}{\phi - \theta_{S\text{-}C}}\right)$$

$$M_C(\theta) = p\left(\frac{2}{15}a\left(9b^2 + 18bc + 4c^2\right) + \frac{1}{2}\pi ab^2\right)$$

$$M_F(\theta) = M_{\max} - \left(\frac{M_{\max} - M_C(\theta_{C\text{-}F})}{\theta_{C\text{-}F}}\right)\theta$$

$$\theta_{C\text{-}F} = \theta' \quad \text{s.t.} \quad \left\{\frac{M_C(\theta') - M_{\max}}{\theta'} = \left(\frac{dM_C}{d\theta}\right)\bigg|_{\theta'}\right\}$$

$$\theta_{S\text{-}C} = \arg\min_\theta(W) \quad \text{s.t.} \quad \{\delta(\theta) = \delta_{\max}\}$$

9

and:

$$a = \frac{1}{6\pi}\left(3s - 4\pi b + \sqrt{3s^2 + 12\pi bs - 20\pi^2 b^2}\right)$$

$$b = \frac{1}{2}\left(2R\csc\frac{\theta}{2} + d + \delta_{\max} - \tilde{L}\right)$$

$$c = 2R\csc\frac{\theta}{2} - 2b$$

$$d = \frac{L}{2} - 2R\cot\frac{\theta}{2}$$

$$s = \pi\left(3(R + \tilde{R}) - \sqrt{\left(3R + \tilde{R}\right)\left(3\tilde{R} + R\right)}\right)$$

$$\tilde{L} = \frac{L}{2} - 2R\cot\frac{\phi}{2}$$

$$\tilde{R} = R\csc\frac{\phi}{2}$$

$$W = 2\pi Rt\left(\frac{5p^2R^2}{8Et^2} + \frac{G\delta^2}{\pi^2R^2}\right)\left(L - 2R\cot\frac{\theta}{2} + \delta\right) + p\pi R^2\left(\delta - 2R\left(\cot\frac{\theta}{2} - \cot\frac{\phi}{2}\right)\right)$$

$$\delta(\theta) = \arg\min_{\delta}(W(\theta))$$

$$\delta_{\max} = 2R\left(\cot\frac{\theta}{2} - \cot\frac{\phi}{2}\right)$$

$$M_{\max} = \frac{p\pi RL^2}{8}$$

S3.6 Model Performance

To verify the validity of our model, in Figure S5 we plot the model predictions against experimental data for all of the actuators fabricated. In general, the model appears to capture the trends observed experimentally and exhibits reasonably close correlation with the experimental data despite the simplicity of the geometry assumptions made. In particular, both the model and experiments show that increases in length primarily serve to increase $M_{\max}$ (Figure S5(b)), increases in pattern angle serve to increase $\theta_{S\text{-}C}$ (Figure S5(d)), and increases in radius increase torque production across all three regimes (Figure S5(c)). Likewise, torque increases linearly with pressure (Figure S5(a)).

The original objective of this model was to provide a first-order approximation of the actuator response to validate our understanding of the underlying phenomena. In particular, the results suggest that the first moment of area method utilized in the model corresponds to the actual mechanism of torque production in the actuators. Thus, it is expected that with a more refined estimation of the cross sectional geometry, a better correspondence with the experimental data could be achieved. This insight can be applied to other similar actuators in the future, providing a simple technique to predict the approximate loads exerted by a fluidic soft actuator. Specifically, in order to maximize actuator torque production at a given angle, one must seek to increase the first moment of area.
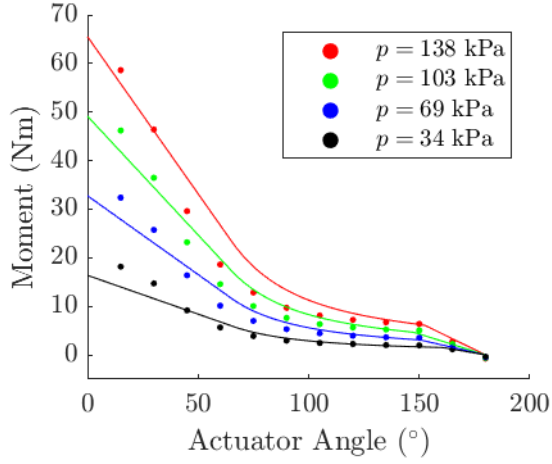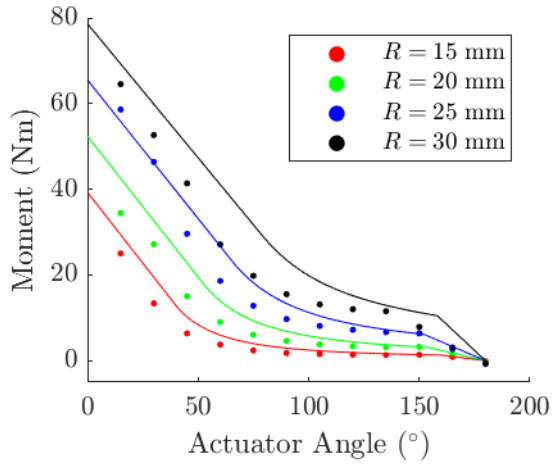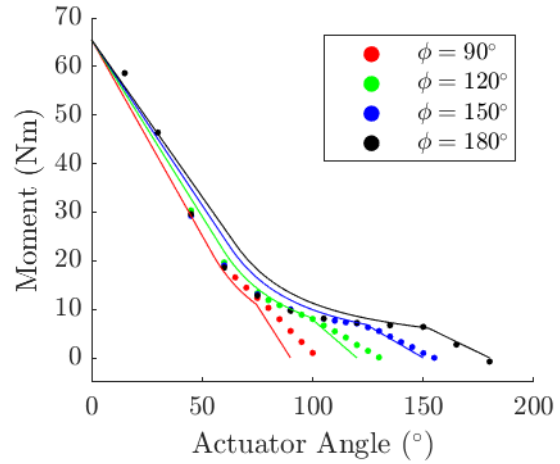
(a) Pressure variations with $R = 25$ mm, $L = 220$ mm, and $\phi = 180°$
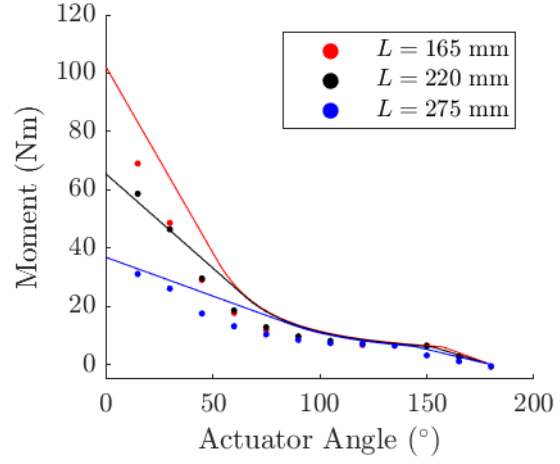
(b) Length variations with $R = 25$ mm and $\phi = 180°$

(c) Radius variations with $L = 220$ mm and $\phi = 180°$

(d) Pattern angle variations with $R = 25$ mm and $L = 220$ mm

Figure S5: Comparison of model predictions (lines) with experimental results (points) for all actuators fabricated.